# Influence of Shear Flow on the Specific Volume and the Crystalline Morphology of Isotactic Polypropylene

**Maurice H. E. Van der Beek,[†,§] Gerrit W. M. Peters,[*,‡] and Han E. H. Meijer[‡]**

*Department of Design and Manufacturing, TNO Science and Industry, P.O. Box 6325, 5600 HE Eindhoven, The Netherlands, and Faculty of Mechanical Engineering, Section Materials Technology, Eindhoven University of Technology, P.O. Box 513, 5600 MB, Eindhoven, The Netherlands*

*Received September 2, 2005; Revised Manuscript Received January 3, 2006*

ABSTRACT: The influence of shear flow on the temperature evolution of the specific volume and the crystalline morphology of two iPP's, differing in weight-averaged molar mass $\bar{M}_w$, was investigated at nonisothermal conditions and elevated pressures, using a custom-designed dilatometer. These conditions are typically in the range of conditions as experienced during polymer processing. A pronounced influence of flow on the temperature marking the transition in specific volume and the rate of transition could be observed. In general, this influence increased with increasing shear rate, decreasing temperature where flow was applied, increasing pressure, and increasing weight-averaged molar mass $\bar{M}_w$ of the polymer. Although the degree of orientation and the overall structure of the resulting crystalline morphology were greatly affected by the flow, the resulting specific volume was only little affected by the thermomechanical conditions presently investigated. Finally, when flow was applied at sufficiently high temperature, in some cases the polymer was able to fully erase the effect of flow. This is attributed to remelting of the flow-induced crystalline structures.

## 1. Introduction

During processing operations such as injection molding, extrusion, fiber spinning, etc., polymers are subjected to different types of flow fields (shear, extension, mixed).[1] For semicrystalline polymers, it is known that these flow conditions strongly influence the process of crystallization and the resulting crystalline morphology.[2−14] This is expected to also have a major influence on the evolution of specific volume and on the final mechanical and dimensional shape properties. The number of studies regarding the influence of flow on the specific volume of polymers is however limited. Fritzsche and Price[15] used a concentric cylinder dilatometer to quantitatively follow the crystallization process of poly(ethylene oxide) (PEO) grades as a function of undercooling, shear rate, and molecular weight. This was derived from specific volume data. Steady shear experiments, with shear rates applied up to 140 1/s, were performed at isothermal conditions and atmospheric pressure. Results showed the start in crystallization, i.e., the transition in the specific volume, to occur at smaller times with increasing shear rate, increasing molecular weight, and higher undercooling. Fleishmann and Koppelmann[16] performed injection molding experiments and compared measured cavity pressure levels with calculated pressure to draw conclusions with respect to the dependence of specific volume on applied flow. The agreement of calculated and experimental pressure data showed large deviations if standard "slow cooling PVT data" were used as input for the model. A better agreement was obtained by shifting the transition temperature of specific volume toward higher temperatures to correct for the influence of flow. Watanabe et al.[17] used a dilatometer consisting of a mixture of a conventional piston−die dilatometer and a plate−plate rheometer to study the influence of (steady) shear rate and elevated pressure at isothermal conditions on the relative degree of crystallinity as derived from specific volume data. The start of the transition in the specific volume of iPP was found to occur at smaller times with increasing shear rate and with increasing pressure. The influence of pressure was explained by the shift in the experimental melting temperature $T_m$ toward higher temperatures, leading to increased undercooling at a constant temperature. Unfortunately, only shear rates up to 0.5 1/s were applied at a maximum pressure of 20 MPa. These conditions are not very representative for the processing conditions as encountered during, for instance, injection molding. Moreover, the plate−plate geometry is not very well suited to study the influence of shear rate on specific volume because of the dependence of shear rate on the sample radius; i.e., it is varying across the sample.

This paper deals with the influence of shear flow on the specific volume and crystalline morphology of isotactic polypropylene measured at conditions close to industrial processing conditions. The combined influence of shear rate, pressure, cooling rate, and the polymer's molecular weight distribution on the temperature-dependent development of the specific volume is studied, using the technique of dilatometry. The results are explained using the present knowledge of (flow induced) crystallization and are related to the crystalline morphology, as investigated ex situ using wide-angle X-ray diffraction (WAXD) and visualized by scanning electron microscopy (ESEM).

## 2. Experimental Part

**Materials.** The materials used are two commercial isotactic polypropylenes (iPP) with different weight distributions. The first material (iPP-1) is supplied by Borealis (grade HD120MO) and the second material (iPP-2) by DSM (grade Stamylan P 13E10). Figure 1 shows the molecular weight distribution of both materials determined via GPC, and Table 1 lists some main properties of both materials. Notice that the iPP-2 was also used by Swartjes et al.,[14] but our results of GPC characterization are somewhat different. For dilatometer experiments, samples with dimensions 2.5 × 65 × 0.4 mm are prepared by compression molding. First, pellets are melted at atmospheric pressure. Next, the material is compressed for 3 min at 210 °C with a force of 50 kN. The samples are cooled

† TNO Science and Industry.
‡ Eindhoven University of Technology.
§ Present address: Philips Applied Technologies. E-mail: maurice.van.der.beek@philips.com.
* Corresponding author. E-mail: g.w.m.peters@tue.nl.

10.1021/ma051914e CCC: $33.50 
Published on Web 02/03/2006

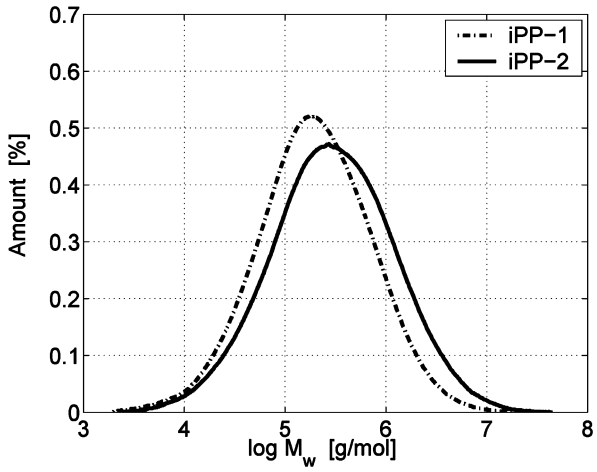


**Figure 1.** Molecular weight distribution determined via gel permeation chromatography (GPC). Data were provided by Gahleitner/Königsdorfer (Borealis, Linz, Austria).

**Table 1. Characterization of the Materials Used in This Study**[a]

| material | $\bar{M}_w$ [g/mol] | $\bar{M}_w/\bar{M}_n$ | $T_m$ [°C] |
|---|---|---|---|
| iPP-1 | 365 000 | 5.2 | 162.7 |
| iPP-2 | 636 000 | 6.9 | 163.0 |

[a] iPP-1: HD120MO (Borealis, Austria); iPP-2: Stamylan P 13E10 (DSM, The Netherlands).

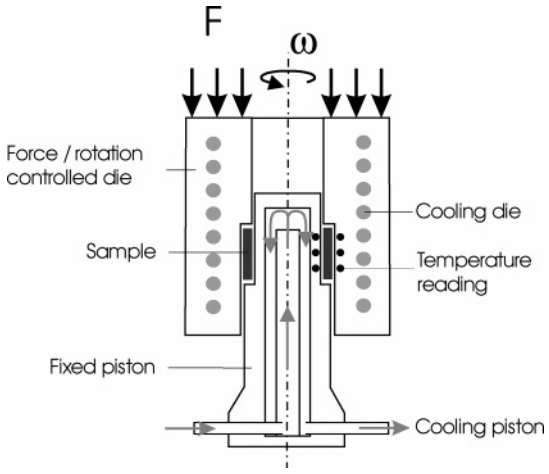


**Figure 2.** Working principle of the custom designed dilatometer.

in a water-cooled press for 5 min from 210 to 25 °C, again with a force of 50 kN.

**Dilatometry.** The influence of shear flow on specific volume at elevated pressures is investigated using the custom-designed dilatometer, as schematically shown in Figure 2. The dilatometer has an annular-shaped sample spacing with an inner radius $r_i$ = 10.50 mm and outer radius $r_o$ = 11.00 mm. The height of the sample can be arbitrarily chosen to a maximum of 10 mm but is here set to 2.0−2.5 mm. Because of this axisymmetric design, the sample can be sheared by rotating the outer part of the device, similar to a Couette rheometer. A more detailed description of the dilatometer is given in Van der Beek et al.[18] where also a comparison was made with specific volume data measured using a conventional "bellows"-type dilatometer, showing relative differences in measured specific volume of 0.1−0.4%.

Dilatometer experiments are performed in the isobaric cooling mode according to the procedure schematically depicted in Figure 3: (A) the sample is heated with an average heating rate of 5 °C/min to a temperature of 210 °C, (B) kept for 10 min at 210 °C to ensure fully melting of the crystalline microstructure, (C) pressurized to the desired level, (D) cooled to room temperature during which the pressure is maintained constant to within ±0.3 MPa,

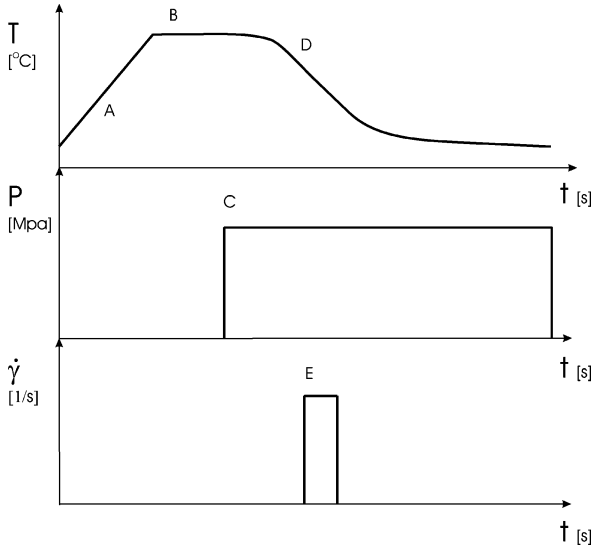


**Figure 3.** Schematic representation of the employed experimental procedure.

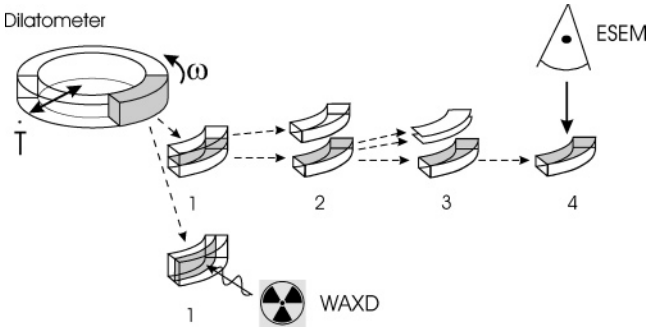


**Figure 4.** Schematic representation of the sample preparation procedure performed on a representative piece cut from the ringlike sample as obtained after the dilatometer experiments (1). For WAXD experiments, no additional sample preparation is performed. For ESEM experiments, this piece is further cut across its approximate center line and parallel to the direction of flow (2). Coupes are taken under cryogenic conditions in order to smoothen the surface (3). The final sample piece is subjected to an acidic solution, and the surface is treated with a gold (Au) layer for visualization by ESEM (4).

and (E) during cooling subjected to shear flow for a certain time and constant shear rate. After the sample is completely cooled, it is taken out of the dilatometer, and the same procedure is repeated in the absence of a sample. This calibration measurement is used to correct the measured volumetric change of the sample for external influences such as thermal expansion of the dilatometer, deformation of the dilatometer due to mechanical loading, etc. Within minutes after finishing the experiments, the samples are removed from the dilatometer and stored in a freezer at −5 °C for later analysis of the crystalline morphology and resulting density.

**Density Gradient Column.** Density gradient column (DGC) experiments were performed according to ASTM D1505, establishing a linear density distribution ranging from 0.87 to 0.94 g/cm$^3$ using water and 2-propanol (IPA). Measurements were performed at a column temperature of 23 °C. Prior to submergence into the column, samples were subjected to an ultrasonic bath, consisting of a representative mixture of water and 2-propanol, for 20 min in order to minimize the presence of air bubbles on the sample surface. From each ring-shaped sample from the PVT measurements, two small samples from different locations were obtained in order to get an indication of the homogeneity of the ring-shaped sample.

**X-ray Analysis.** Wide-angle X-ray diffraction (WAXD) experiments were performed ex-situ at the materials beamline ID 11 of the European Synchrotron Radiation Facility (ESRF) in Grenoble, France. Actual experiments were performed on a representative piece of the ringlike samples that results from dilatometer experi-

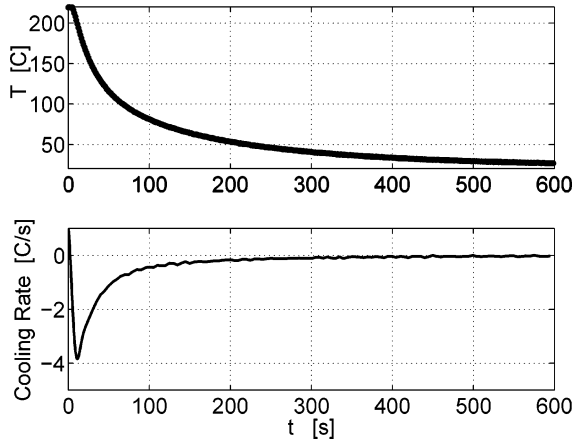


**Figure 5.** Recorded temperature (top) and derived cooling rate (bottom).

ments (Figure 4). The size of the X-ray beam is 0.2 × 0.2 mm$^2$, having a wavelength of 0.4956 Å. The beam passes through the sample in a direction parallel to the initial direction of cooling and perpendicular to the direction of applied flow. Because the curvature of the sample is much larger than the dimensions of the beam, the effect of this curvature on the diffraction pattern is assumed negligible. The detector used is a Frelon CCD detector with 1024 × 1024 pixels. Both horizontal and vertical pixels are 164 $\mu$m in size. From calibration experiments, using lanthanum hexaboride, a sample-to-detector distance of 439.9 mm was determined. The exposure time for all images was 30 s.

**Table 2. Temperatures $T_\gamma$ Where Shear Flow Is Applied and Associated Undercooling $\Delta T_\gamma$ for Both IPP's**

| iPP-1 | | iPP-2 | |
|---|---|---|---|
| $T_\gamma$ [°C] | $\Delta T_\gamma$ [°C] | $T_\gamma$ [°C] | $\Delta T_\gamma$ [°C] |
| 139 | 59.2 | 133 | 65.2 |
| 154 | 44.2 | 153 | 45.2 |
| 193 | 5.2 | 193 | 5.2 |

**Scanning Electron Microscopy.** For scanning electron experiments (ESEM), a representative piece is taken from the ringlike sample that results from dilatometer experiments and cut across its approximate center line and parallel to the direction of applied flow (Figure 4). The surface of one of the sample halves is smoothed by taking microtome cuts under cryogenic conditions. The final sample was subsequently etched for 4 h in a mixture of potassium permanganate ($KMnO_4$) and acid (4 vol % $H_3PO_4$, 10 vol % $H_2SO_4$) and coated with gold (Au). Finally, imaging of the etched sample surface was done with a Philips XL30 ESEM using a SE detector and operated at 5 kV.

## 3. Results and Discussion

**Specific Volume.** Dilatometer experiments were performed to study the combined influence of shear flow, pressure, and

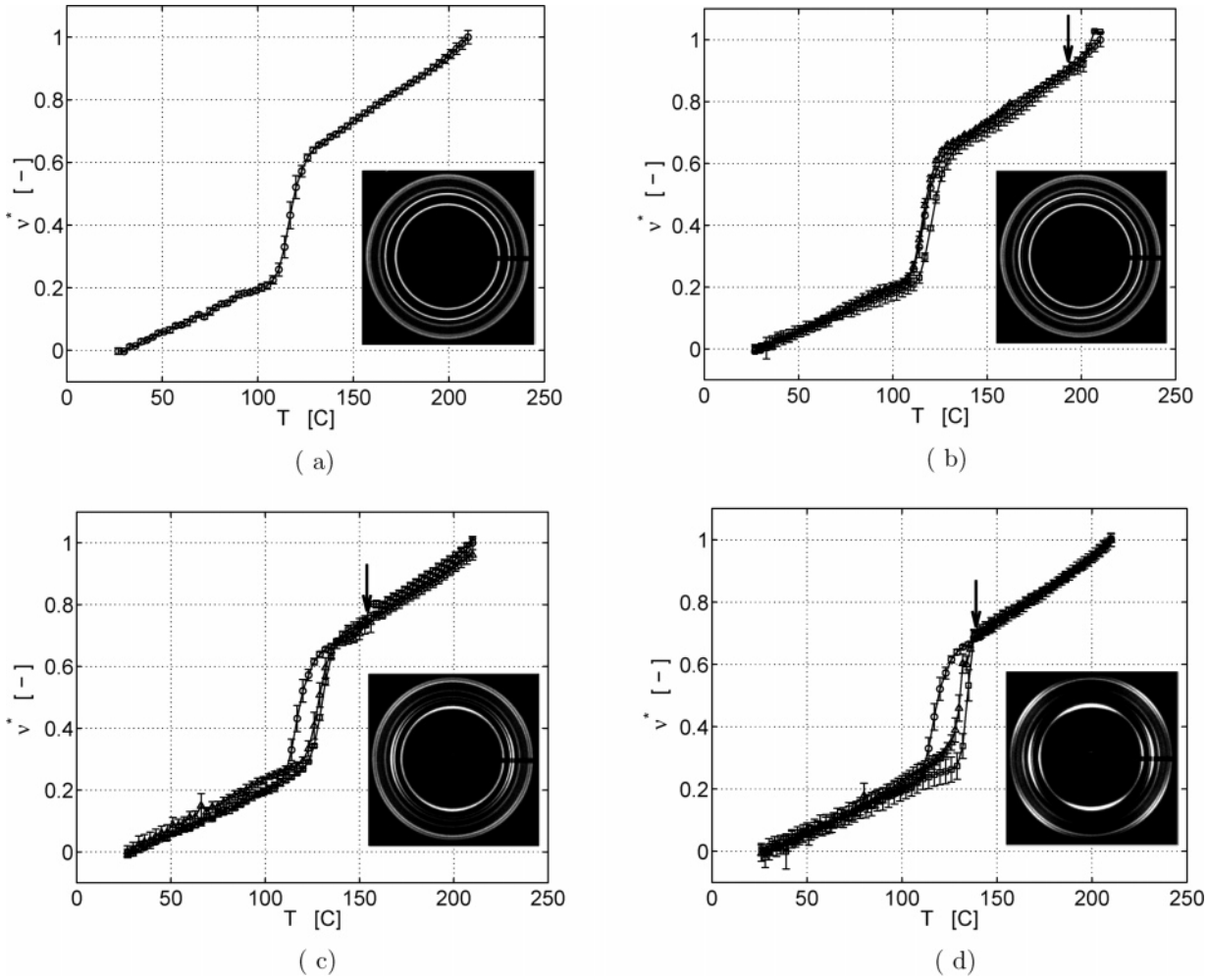


**Figure 6.** Influence of shear flow on the normalized specific volume $v^*$ of iPP-1. Shear flow is applied as a step function with a shear rate of 39.0 1/s for 3.0 s (△) or a shear rate of 78.0 1/s for 1.5 s (□) at various temperatures, indicated by the arrows: (a) no shear flow applied, (b) $T_\gamma$ = 193 °C, (c) $T_\gamma$ = 154 °C, (d) $T_\gamma$ = 139 °C. Measurements performed in absence of flow are represented by (○). All measurements are performed at a constant pressure of 40 MPa. WAXD images show the influence of shear flow on the orientation of the resulting crystalline morphology, using a shear rate of 39.0 1/s for 3.0 s.

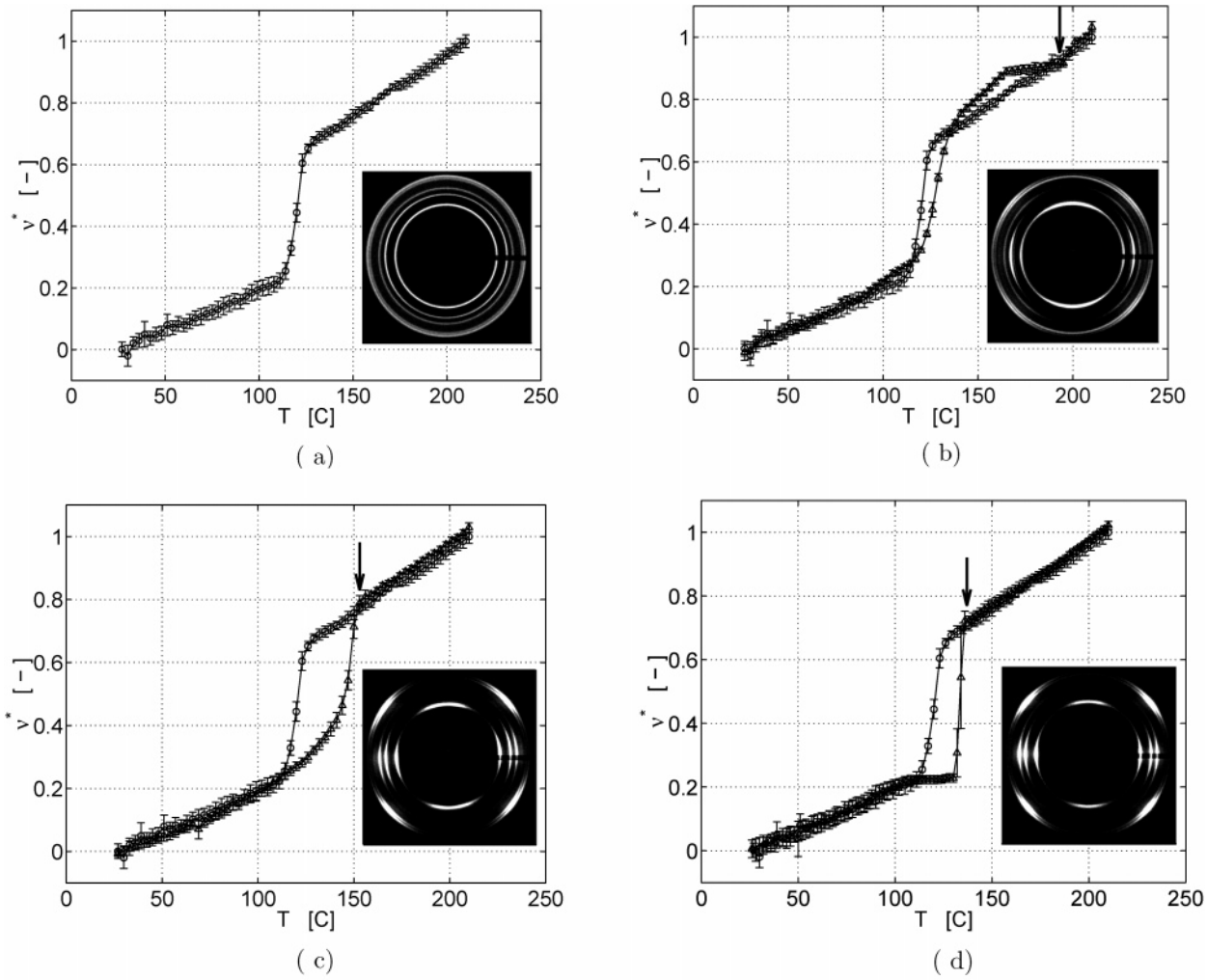


**Figure 7.** Influence of shear flow on the normalized specific volume $\nu^*$ of iPP-2. Shear flow is applied as a step function with a shear rate of 39.0 1/s for 3.0 s (Δ) at various temperatures, indicated by the arrows: (a) no shear flow applied, (b) $T_\gamma = 193$ °C, (c) $T_\gamma = 153$ °C, (d) $T_\gamma = 133$ °C. Measurements performed in the absence of flow are represented by (○). All measurements are performed at a constant pressure of 40 MPa. WAXD images show the influence of shear flow on the orientation of the resulting crystalline morphology.

molecular parameters on the specific volume of iPP. Parameters varied are (a) average temperature during flow, (b) shear rate at constant total shear, (c) the molecular weight distribution (MWD) of the polymer, and (d) pressure during flow. In the following analysis of the results, the specific volume is normalized to make comparison of results obtained at various processing conditions more easy. The normalized specific volume $\nu^*$ is defined as

$$\nu^* = \frac{\nu - \nu_s}{\nu_m - \nu_s} \tag{1}$$

where $\nu$ is the measured specific volume, $\nu_s$ is the value of the specific volume in the solid state at room temperature (in case the sample was not subjected to flow), and $\nu_m$ represents the value of the specific volume in the melt state at 210 °C.

**Influence of Temperature during Flow.** The influence of the thermomechanical history on the specific volume of iPP was investigated by subjecting the polymer to shear flow at various temperatures. The pressure during the experiments was kept constant at 40 MPa, and cooling as depicted in Figure 5 was applied. Typically, the cooling rate during crystallization of the polymer was about 1.4−2.0 °C/s. Shear flow was applied as a step-function during cooling, with a shear rate $\dot\gamma = 39.0$ 1/s for a shear time $t_s = 3.0$ s or $\dot\gamma = 78.0$ 1/s for $t_s = 1.5$ s; i.e., the total shear is approximately constant. Flow was applied at various temperatures, i.e., different degrees of undercooling. Since shear flow was applied during cooling over a small temperature range, the averaged value of this range is taken as a characteristic value and further referred to as $T_\gamma$. Values for $T_\gamma$ and the associated undercooling, $\Delta T_\gamma = T^0_m - T_\gamma$, are listed in Table 2. For the equilibrium melting temperature $T^0_m$ at a pressure of 40 MPa, a value of 198.2 °C is used.[19]

Figures 6 and 7 show the influence of shear flow applied at various temperatures $T_\gamma$ on the normalized specific volume of respectively iPP-1 and iPP-2. Arrows indicate the temperature $T_\gamma$ where flow is applied. The WAXD patterns give an indication of the orientation of the resulting crystalline morphology (flow direction is vertical). Furthermore, in each subfigure the specific volume measured in the absence of flow is incorporated for reference. From Figure 6 it is observed that, depending on $T_\gamma$, shear flow can have a profound influence on the temperature $T_t$ marking the onset of the transition, whereas the specific volume of the solid state is hardly affected. If shear flow has an effect, then $T_t$ shifts toward higher temperatures, and associated with this WAXD analysis shows arcing of the Debye−Scherrer rings. This is an indication for orientation of the resulting crystalline morphology. From a thermodynamic point of view, the shift in $T_t$ toward higher temperatures can be explained from the orientation of polymer chains due to shear

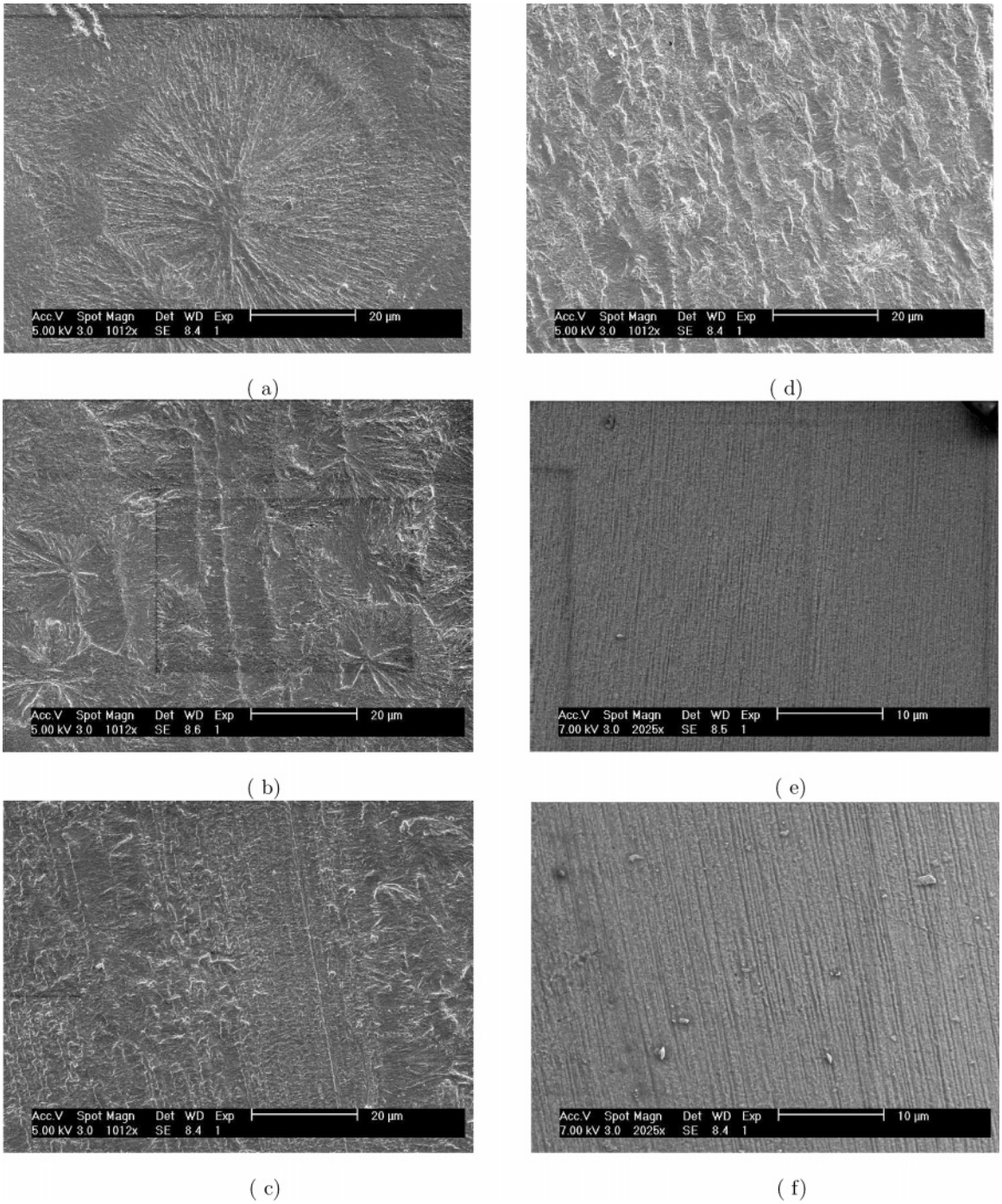


**Figure 8.** Crystalline morphology close to the core of the samples using ESEM. Flow direction is vertical. Pictures a−c correspond to iPP-1 subjected to a shear rate of 39.0 1/s for 3.0 s applied at $T_\gamma = 193$ °C (a), $T_\gamma = 154$ °C (b), and $T_\gamma = 139$ °C (c), respectively. Pictures d−f correspond to iPP-2 and $T_\gamma = 193$ °C (d), $T_\gamma = 153$ °C (e), and $T_\gamma = 133$ °C (f), respectively. The direction of applied flow is vertical (see also Figure 4).

flow, causing a decrease in melt entropy. This can be reflected in an effective increase of the melting temperature.[20] At a given temperature the effective undercooling $\Delta T$ is therefore higher. From a crystallization kinetics point of view, molecular orientation yields an enhanced formation of (flow induced) primary nuclei.[2,3,6,9,11,21] The number of flow-induced nuclei can be some orders of magnitude higher than the number of nuclei formed at quiescent conditions.[13] Both effects will enhance the crystallization kinetics, enabling the process of crystallization to start at higher temperatures. Furthermore, with increasing $T_\gamma$ the resulting crystalline morphology shows less orientation, and the temperature interval between $T_\gamma$ and $T_t$ increases. Note that if iPP-1 is subjected to a shear rate of $\dot{\gamma} = 39.0$ 1/s at $T_\gamma = 193$ °C, the effect of flow on the resulting orientation of the crystalline morphology is erased (Figure 6b). This ability of the melt to erase the influence of flow was also observed by others[22,26,27] and is attributed to remelting of the flow-induced crystalline structure and relaxation of oriented chains. However, the crystalline morphology does show differences compared to the morphology resulting from quiescent crystallization, i.e., a higher fraction of $\beta$-crystals (see Figure 14). If the same polymer is subjected to a shear rate of $\dot{\gamma} = 78.0$ 1/s at $T_\gamma = 193$ °C, the influence of flow is not fully erased as indicated by a small shift in $T_t$ (see Figure 6b).

If shear flow is applied at increased undercooling (Figure 6c,d), remelting of flow-induced structures can be ignored.[22]

The evolution of the specific volume in case the polymer is subjected to $\dot{\gamma} = 39.0$ 1/s applied at either $T_\gamma = 154$ °C or $T_\gamma = 139$ °C matches surprisingly well. The temperature marking the start of the transition and the evolution of the transition itself are almost identical. If the temperature at which shear flow is applied is taken as a reference, the polymer needs an additional undercooling of about 17 °C for the transition to start in case shear flow is applied at $T_\gamma = 154$ °C. If shear flow is applied at $T_\gamma = 139$ °C, the transition starts almost immediately; i.e., the time needed to start crystallization after application of flow reduces. There are several reasons for that. First, viscoelastic stresses arising from shear flow at lower temperature are higher, therefore leading to a higher number of shear-induced nuclei.[13] Second, at lower $T_\gamma$, or higher undercooling $\Delta T_\gamma$, a larger number of quiescently formed nuclei are present, which are believed to link molecules into a physical network.[23] Shear flow applied will thus have a larger orienting effect throughout the melt, potentially forming more flow-induced nuclei. Third, the spherulitic growth rate is larger at higher undercooling. These effects explain the enhanced crystallization process from the moment flow is applied and the higher degree of orientation visualized by WAXD in Figure 6d compared to Figure 6c. This agrees qualitatively with the resulting crystalline morphology as visualized by ESEM (Figure 8). Pictures a−c correspond to iPP-1 and show the influence of flow applied at various temperatures $T_\gamma$. All images are taken close to the core of the sample. When shear flow is applied at lower $T_\gamma$, smaller spherulites are formed and the orientation of the morphology increases (row nucleation). Figure 6d furthermore shows that by increasing the shear rate to $\dot{\gamma} = 78.0$ 1/s the crystallization kinetics are more enhanced; i.e., the whole transition process takes place much faster.

Finally, Figure 9a shows the influence of $T_\gamma$ on the resulting specific volume measured via DGC. The specific volume resulting from quiescent conditions, i.e., no shear flow applied, is represented by filled symbols plotted at the highest temperature $T_\gamma$. The lines are drawn to guide the eye and are not based on statistical analysis because the number of experimental data points is too low. In general, the influence of shear flow on the resulting specific volume can be neglected—this despite the observed differences in the evolution of specific volume and differences in the orientation and structure of the crystalline morphology.

Note: in an earlier study,[25] we analyzed the influence of cooling rate on the specific volume of iPP-1 in quiescent conditions. We concluded that the average cooling rate during crystallization could be used as a measure to characterize the influence of the nonisothermal cooling conditions employed in our experiments on the evolution of specific volume. In our current shear flow experiments, the average cooling rate during crystallization varies slightly between the experiments because flow is applied during cooling. During quiescent conditions, the cooling rate is about 1.4 °C/s, while in shear flow experiments this varies from 1.4 °C/s (shearing iPP-1 at 193 °C, Figure 6b) to a maximum 2.0 °C/s (shearing iPP-2 at 154 °C, Figure 7c). From this same study, we can conclude that a difference in cooling rate of 1.4−2.0 °C/s causes a shift in $T_t$ of about 1.1 °C toward lower temperatures during quiescent crystallization. This is far less than the shift in $T_t$ toward higher temperatures resulting from the applied shear flows. Therefore, the relatively small differences in cooling rate during crystallization are assumed to be negligible.

**Influence of Molar Mass Distribution.** Figure 7 shows the influence of $T_\gamma$ on the normalized specific volume and resulting

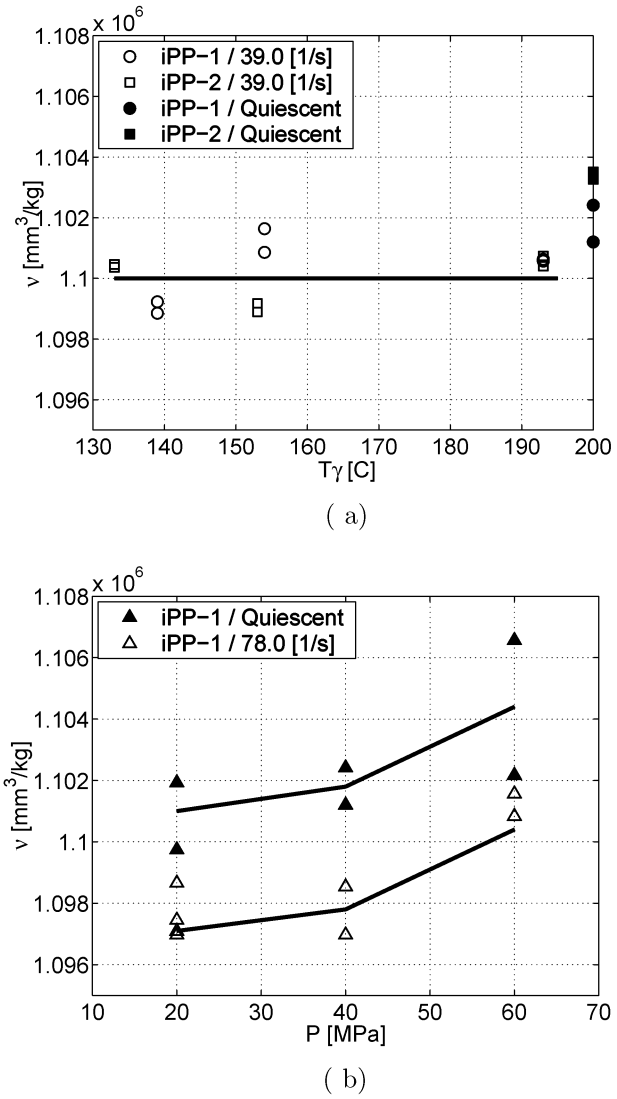


**Figure 9.** (a) Influence of shear flow applied with a shear rate of 39.0 1/s for 3.0 s at a pressure of 40 MPa for various $T_\gamma$ on the specific volume after complete cooling. (b) Influence of pressure on the resulting specific volume of iPP-1 when shear flow is applied with a shear rate of 78.0 1/s for 1.5 s at $T_\gamma = 140$ °C. Lines are used to guide the eye.

crystalline morphology of iPP-2. With respect to iPP-1, this material has a higher weight-averaged molar mass $\bar{M}_w$. Comparing Figures 6a and 7a, we conclude that the normalized specific volume of both (polydisperse) iPP's at quiescent conditions is practically identical. As expected, the effect of shear flow on the specific volume and the resulting crystalline morphology is significantly enhanced by the presence of longer chains.[4,7,8,10,12,26] If shear flow is applied to the undercooled melt of iPP-2, the transition to the semicrystalline state is significantly faster (Figure 7d), or the temperature interval between $T_\gamma$ and $T_t$ decreases compared to the iPP-1 results (Figure 7c). Even when shear flow is applied at $T_\gamma = 193$ °C, i.e., close to the equilibrium melting temperature $T_m^0$, the specific volume and crystalline morphology are affected (Figure 7b).

Figure 8d−f again confirms the pronounced influence of the number of long chains on the crystallization kinetics after flow. Contrary to iPP-1, significant orientation of the morphology is already seen when shearing at $T_\gamma = 193$ °C (Figure 8d), which was already observed in the WAXD patterns in Figure 7. With decreasing temperature of flow, bundles of highly oriented structures can be observed at $T_\gamma = 154$ °C, and finally a densely

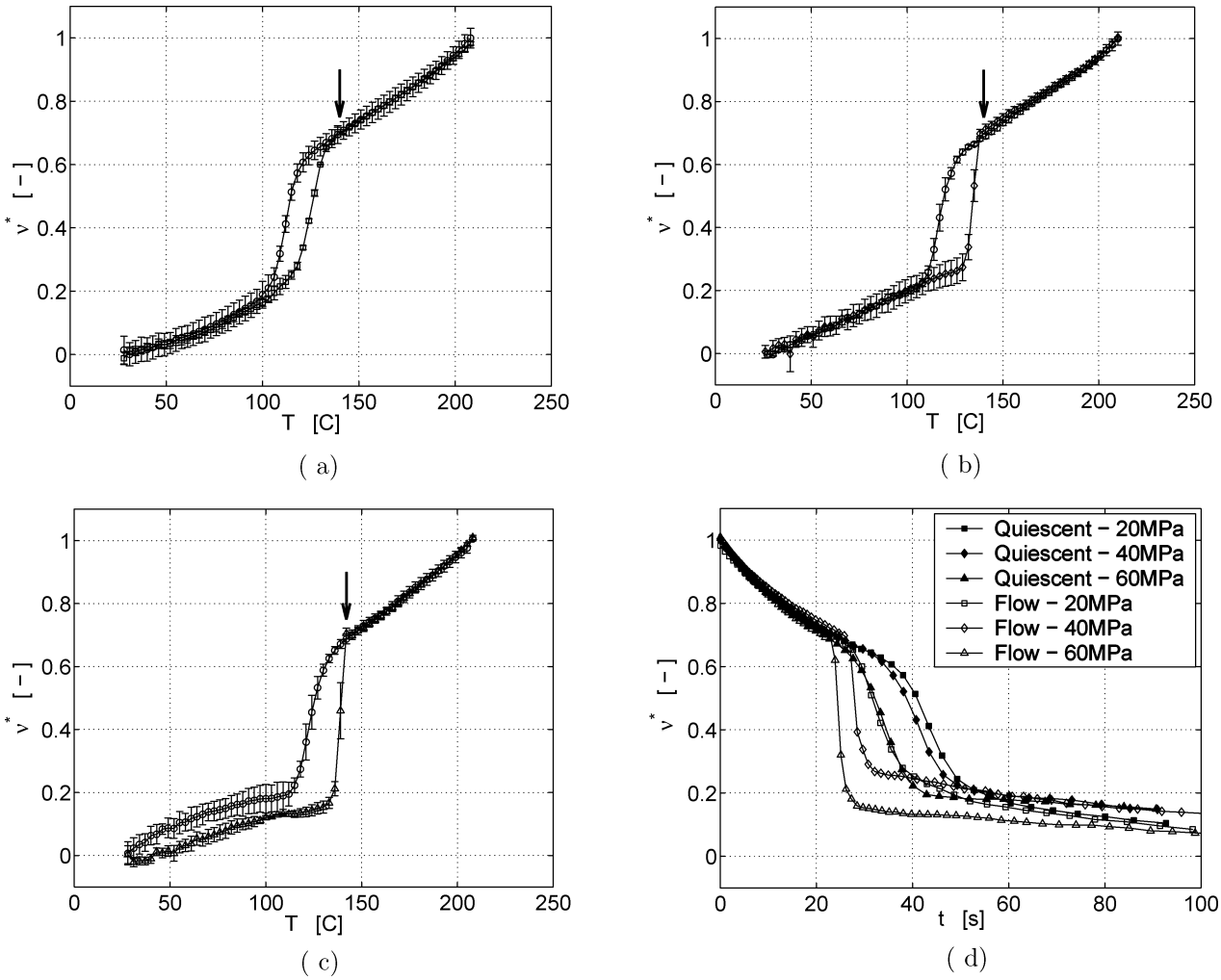


**Figure 10.** Influence of the pressure during shear flow on the normalized specific volume of iPP-1. Shear flow is applied as a step function with a shear rate of 78.0 1/s for 1.5 s at $T_\gamma = 140$ °C. Pressure levels are (a) 20, (b) 40, and (c) 60 MPa. Normalized specific volume as a function of time is shown in (d) and illustrates the effect of pressure on the rate of crystallization.

packed highly oriented structure results across the whole sample thickness in the case of $T_\gamma = 139$ °C.

Finally, the influence of $T_\gamma$ on the specific volume after complete cooling (Figure 9a) shows the same trend as for iPP-1. The molecular weight distribution seems to play a minor role in this.

**Influence of Pressure during Flow.** The influence of the pressure during flow is investigated for iPP-1, either for a constant temperature $T_\gamma$ or for a constant undercooling $\Delta T_\gamma$. In both cases the polymer is subjected to a shear rate of 78.0 1/s during 1.5 s at pressure levels 20, 40, and 60 MPa. Figure 10 shows the results if shear flow is applied at $T_\gamma = 140$ °C. All pressure levels display the typical shift of $T_t$ toward higher temperatures while the effect on the specific volume of the solid state is small to negligible. Additionally, we see the small temperature interval between $T_\gamma$ and $T_t$ to decrease even further with increasing pressure, and the transition in specific volume is getting more abrupt. These last observations point to enhancement of the crystallization process after and during flow with increased pressure level. If the specific volume is analyzed as a function of time (see Figure 10d), an increase in the transition rate is observed with respect to the quiescent situation by a factor 1.4, 4.6, and 6.0 for pressure levels of 20, 40, and 60 MPa, respectively. Figure 9b shows the specific volume after complete cooling, measured with DGC. Lines are used to guide the eye. The increase in specific volume with formation pressure

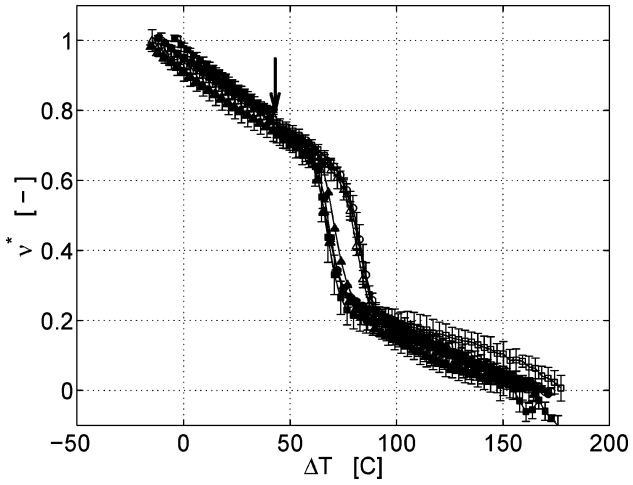


**Figure 11.** Influence of pressure on the normalized specific volume when applying a step shear of 78.0 1/s for 1.5 s at a undercooling $\Delta T_\gamma = 41.9-44.6$ °C (see text for explanation). Pressure levels are (△) 20, (○) 40, and (□) 60 MPa. Specific volume measured at quiescent conditions is represented by open symbols, while the filled symbols represent specific volume subjected to shear flow.

confirms results of La Carrubba et al.[24] and for various cooling rates was earlier published by us.[25] The decrease in specific volume with respect to quiescent conditions is the same for every pressure level applied, about 0.28−0.29%.

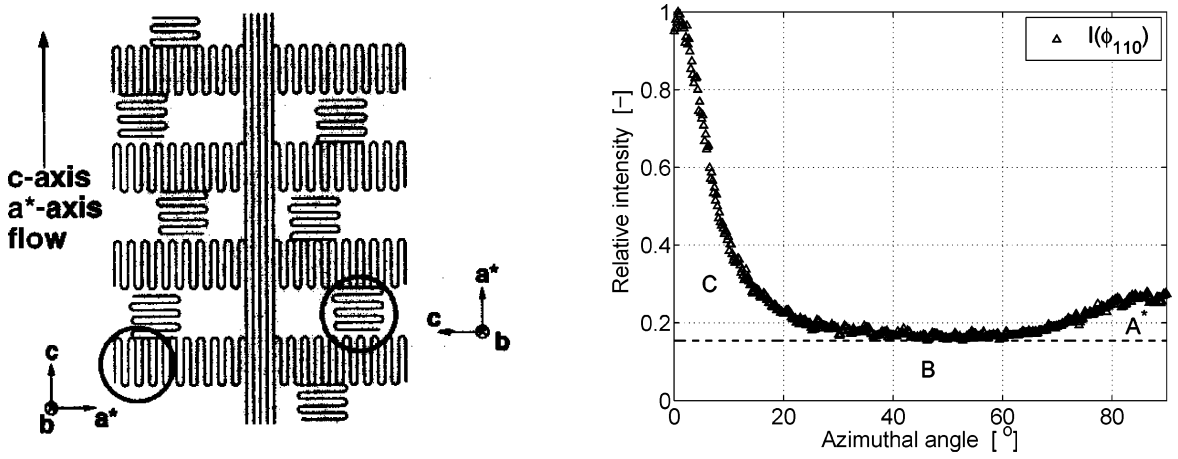


**Figure 12.** (a) Lamellar branched shish-kebab structure.[30] (b) Method to determine fraction [*A**] from the relative intensity of the (110) reflective plane according to Fujiyama.[29]

Figure 11 shows the influence of shear flow applied on the specific volume measured at pressure levels 20, 40, and 60 MPa and an almost identical undercooling. Because of the pressure dependence of the equilibrium melting temperature $T_m^0$ of iPP,[19] the temperature at which the flow is applied increases with increasing pressure. For pressure levels 20, 40, and 60 MPa, the temperature where flow is applied $T_\gamma$ is 150.1, 153.6, and 160.7 °C, respectively. Using the data of Mezghani and Philips[19] for the pressure dependence of iPP's $T_m^0$, this resulted in an undercooling during flow of 41.9, 44.6, and 43.1 °C, respectively. For all pressure levels we see an identical shift of $T_t$ with respect to quiescent conditions (open symbols). Also, the transition itself shows hardly any differences between the various pressure levels.

In Figure 10, the transition from the amorphous to the semicrystalline state occurs in a smaller temperature interval when flow is applied at higher pressure. Because the cooling rate during these experiments is about the same, this implies an increased rate of crystallization. One of the reasons for this increased rate of crystallization is the increased undercooling at which flow is applied because of the pressure dependence of the melting temperature. Since undercooling is the actual driving force for (quiescent) crystallization, at a higher undercooling, (i) flow is applied to a melt containing a larger number of quiescent nuclei, which possibly link molecules to a larger network[23] and thus lead to a higher orientation resulting from the flow further enhancing the effect of flow on the process of crystallization, and (ii) the growth rate of quiescent and flow-induced nuclei is higher, leading to an enhanced rate of crystallization. When flow is applied at relatively large undercooling such as in our experiments, relaxation of molecules after cessation of flow has a minor effect on the process of crystallization.[12] Although the flow is applied at different temperatures in Figure 11, the changing pressure causes the flow to be applied at almost the same undercooling. This explains the almost identical evolution of the specific volume in this figure.

**3.1. Crystalline Morphology. Degree of Orientation.** The degree of crystal orientation, visualized by WAXD analysis in Figures 6 and 7, can be further quantified using the Herman orientation factor *f*. The orientation function is defined as

$$f = \frac{3\langle\cos^2\phi\rangle - 1}{2} \tag{2}$$

where $\phi$ is the angle between a reference direction (e.g., the direction of applied flow) and the normal to a set of *hkl* reflective planes. The term $\langle\cos^2\phi\rangle$ is defined as

$$\langle\cos^2\phi\rangle = \frac{\int_0^{\pi/2} I(\phi)\cos^2\phi\sin\phi\,\mathrm{d}\phi}{\int_0^{\pi/2} I(\phi)\sin\phi\,\mathrm{d}\phi} \tag{3}$$

where $I(\phi)$ is the pole concentration representing the relative amount of crystalline material having plane normals in the direction of $\phi$, $\psi$ such that

$$I(\phi) = \int_0^{2\pi} I(\phi,\psi)\,\mathrm{d}\psi \tag{4}$$

The best and accessible measure for the *c*-axis orientation, the molecular backbone orientation directly related to the flow-induced orientation (and thus flow-induced crystallization), is the orientation of the α-phase (see also Figure 12a). The α-crystalline phase of polypropylene does not have a *hkl* reflective plane which directly reveals the *c*-axis orientation. Therefore, the method of Wilchinsky[28] is used to derive the *c*-axis orientation using the (110) and (040) reflections and the angle of 72.5° between the *b*-axis and the (110) plane. For the angle $\sigma$ between the *c*-axis and the direction of flow, the corresponding $\langle\cos^2\sigma\rangle$ is now calculated according to

$$\langle\cos^2\sigma\rangle = 1 - 0.901\langle\cos^2\phi_{040}\rangle - 1.099\langle\cos^2\phi_{110}\rangle \tag{5}$$

When the *c*-axis is perfectly aligned to the direction of flow, $f = 1$, if the *c*-axis is aligned perpendicular to the direction of flow $f = -1/2$, and for random orientation $f = 0$. For both iPP's, the Herman orientation factor *f* is given in Figure 13 in case shear flow is applied with $\dot{\gamma} = 39.0$ 1/s. Furthermore, to differentiate between *c*-axis orientation and *a**-axis orientation, caused by lamellar branching, the relative fraction of *a**-axis component [*A**] is calculated according to Fujiyama.[29] This fraction can be evaluated from the relative intensity of the (110) reflection vs azimuthal angle, depicted in Figure 12b, following

$$[A^*] = \frac{A^*}{C + A^*} \tag{6}$$

where *C* is taken as the area around an azimuthal angle of 0° and *A** the area around an azimuthal angle of 90°, after subtraction of the baseline area *B*.

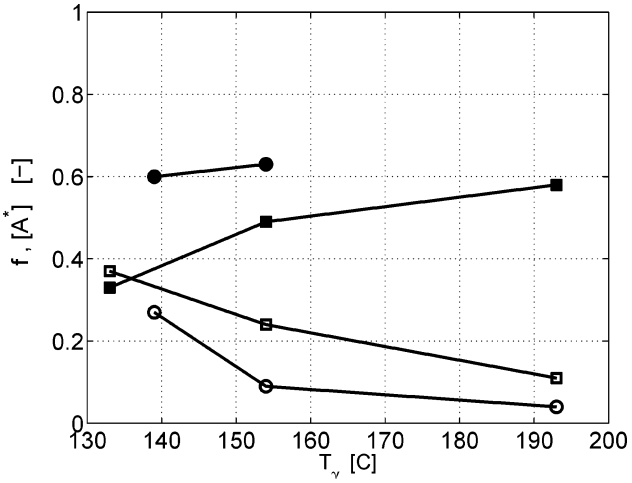


**Figure 13.** Herman orientation factor *f* (open symbols) and the amount (fraction) of lamellar branching expressed by [*A**] (filled symbols) as a function of temperature $T_\gamma$ where flow is applied, at a pressure of 40 MPa: (○) iPP-1; (□) iPP-2.

Figure 13 shows the Herman orientation factor *f* as a function of the temperature $T_\gamma$ where flow is applied with $\dot{\gamma} = 39.0$ 1/s for $t_s = 3.0$ s. For both iPP's, the orientation increases when flow is applied at lower temperatures. Shear flow applied at lower temperature leads to higher viscoelastic stresses, enabling a higher degree of orientation of the molecules. As expected, the higher molecular weight iPP-2 consistently shows higher values for *f*. Because of the corresponding higher rheological relaxation times, molecular orientation resulting from flow prevails for a longer time. Furthermore, the fraction [*A**] decreases with decreasing $T_\gamma$. At lower temperatures, or higher undercooling, the process of flow-induced crystallization is faster, leaving less time for secondary crystallization processes such as lamellar branching. Note that the Herman orientation factor only takes the oriented α-crystals into account, while also a significant amount of *β*-crystals shows orientation in the WAXD images shown in Figures 6 and 7. These $(300)_\beta$ reflections show the same arcing pattern as the $(040)_\alpha$ reflections. The orientation of the *c*-axis of the *β*-crystals can, however, not directly be determined from the $(300)_\beta$ reflection.

**Polymorphism.** The degree of crystallinity and the presence of the crystalline phases (α-monoclinic, *β*-hexagonal, *γ*-orthorhombic) are investigated as a function of $T_\gamma$, for a shear rate of $\dot{\gamma} = 39.0$ 1/s and $t_s = 3.0$ s at a pressure of 40 MPa. From the two-dimensional WAXD images, one-dimensional scattering (1D WAXD) profiles are obtained by integration of the Debye−Scherrer rings along the azimuthal angle. Furthermore, to correct for small variations in sample thickness and fluctuations of the beam, the intensity is normalized such that the area underneath the curve equals unity according to

$$I^*(2\theta) = \frac{I(2\theta)}{\int I(2\theta)\, \mathrm{d}(2\theta)} \tag{7}$$

The degree of crystallinity is determined by subtracting the scattering pattern of a nearly 100% amorphous sample from

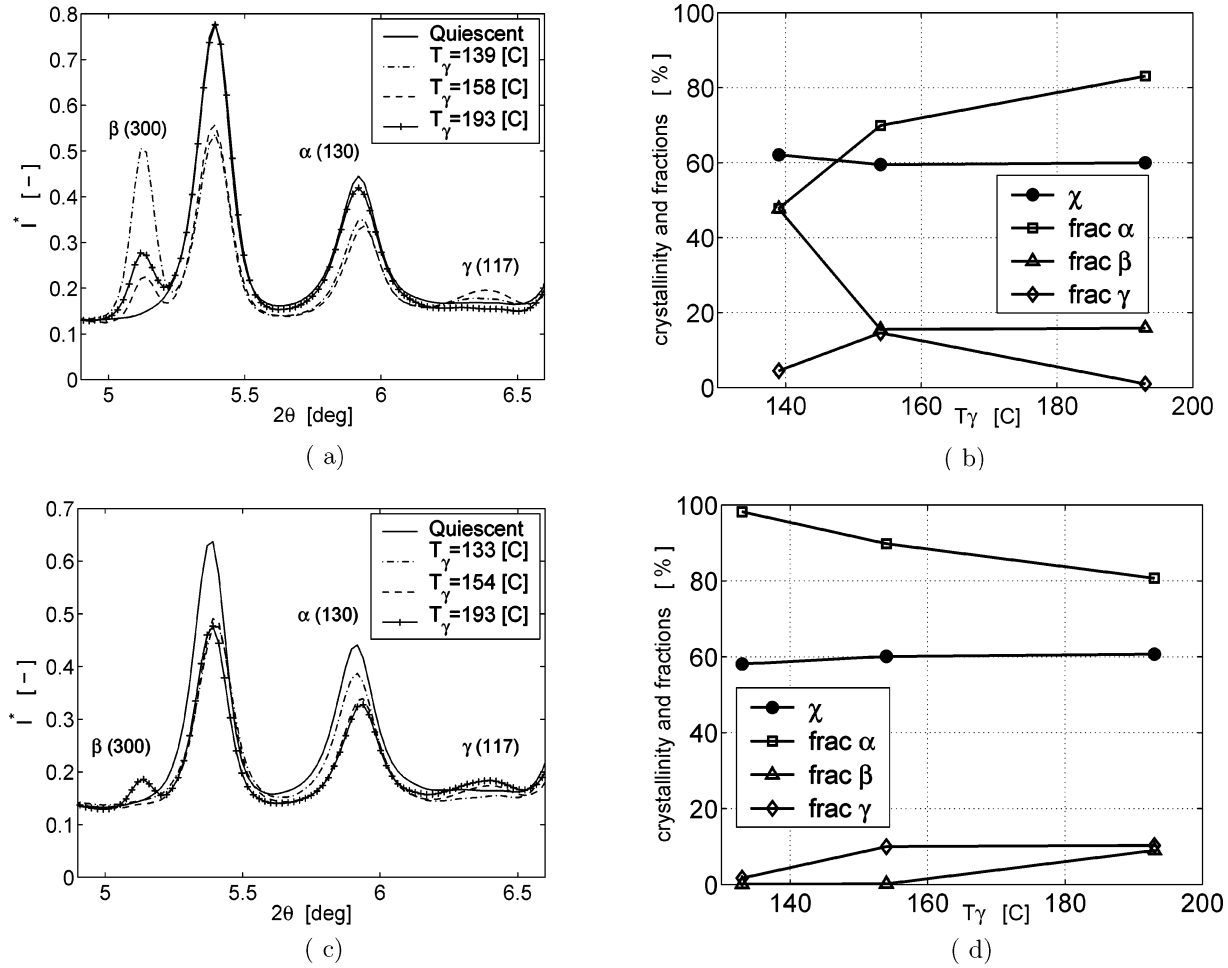


**Figure 14.** 1D-WAXD direction plots showing the normalized intensity *I**, crystallinity *χ*, and relative amounts of the α-, *β*-, and *γ*-crystalline phases dependent on temperature of applied flow: (a, b) iPP-1; (c, d) iPP-2.

the scattering patterns of semicrystalline samples, a method also used for instance by Somani et al.[31] To do this, the intensity is scaled such that the maximum of the amorphous halo equals the minimum between the $(110)_\alpha/(111)_\gamma$ and $(040)_\alpha/(008)_\gamma$ diffraction peaks. Additionally, values for the relative fractions of the crystalline phases in iPP are determined according to the method of Van der Burgt et al.[32] Changes in the $(130)_\alpha$ scattering peak, which is located at $2\theta = 5.94°$ for $\lambda = 0.4956$ Å, are taken as indicative for changes in α-monoclinic crystalline phase. For the $\gamma$-orthorhombic crystalline phase the $(117)_\gamma$ peak at $2\theta = 6.49°$ is used. The relative amount of the $\beta$-crystalline phase is determined from the $(300)_\beta$ diffraction peak, which can be discerned as a shoulder to the $(040)_\alpha/(008)_\gamma$ diffraction peak at approximately $2\theta = 5.14°$ for $\lambda = 0.4956$ Å. The relative fractions are determined from the area beneath the respective scattering peaks in the normalized 1D-WAXD patterns. Figure 14 shows a detail of the 1D-WAXD scattering profiles with the relevant diffraction peaks depicted and the degree of crystallinity with relative amount of crystalline phases. For both iPP's, the degree of crystallinity $\chi$ is hardly affected by shear flow and with a value of about $\chi = 60\%$ very close to the value obtained after quiescent crystallization. The relative amount of $\beta$- and $\gamma$-crystals, next to the more common α-crystals, is however subject to significant changes dependent on the temperature where flow is applied. Figure 14a,b shows the strong increase in relative amount of $\beta$-crystals if iPP-1 is subjected to shear flow at lower temperatures. This relates to the increase in orientation of (α-)crystals, i.e., increase in the Herman orientation factor, which was also found by Somani et al.,[31] as according to refs 33−36 the surface of these oriented α-crystals would provide nucleation sites for $\beta$-crystals to grow. The 2D-WAXD patterns in Figure 6 show an identical arcing pattern for the $(300)_\beta$ and $(040)_\alpha$ reflections. The relative amount of $\gamma$-crystals is also enhanced with respect to quiescent conditions. For iPP-2 (Figure 14c,d), the relative amount of $\beta$-crystals shows however a completely different dependence on the temperature $T_\gamma$—this despite a larger amount of oriented α-crystals as quantified by the Herman orientation factor (Figure 13). For $T_\gamma = 193$ °C, the relative amount of $\beta$-crystals is comparable to the amount present in iPP-1 when sheared at identical temperature. A possible reason for the absence of $\beta$-crystals after shearing at $T_\gamma = 154$ °C and $T_\gamma = 133$ °C could be that the generally weak $(300)_\beta$ reflections are overpowered by the very strong $(040)_\alpha$ reflections. Another reason could be that because of the faster crystallization kinetics, the time is too short for the $\beta$-crystals to grow on the already formed α-crystals.

## 4. Conclusions

The influence of shear flow on the evolution of specific volume of two iPP grades at nonisothermal conditions and elevated pressures was investigated via the technique of dilatometry. In general, shear flow has a pronounced effect on the evolution of specific volume. Especially the temperature marking the transition in specific volume $T_t$ and the rate of transition are affected. The effect of flow on the evolution of specific volume increases with increasing shear rate, increasing pressure, decreasing temperature at which flow is applied, and higher $\bar{M}_w$. A more general classification of the combined effect of these parameters on the evolution of specific volume and resulting crystalline morphology, based on the Deborah number, including a comparison of rheological and experimental time scales, will be address by us in a future publication. Although the degree of orientation and the overall structure of the resulting crystalline morphology were greatly affected by the flow, the resulting specific volume was not significantly affected by the processing conditions employed and shows a clear link to the degree of crystallinity which was also hardly affected by shear flow. It is clear that flow can strongly enhance the occurrence of the $\beta$-crystalline phase. Crystallization models consisting of one crystalline phase are therefore most probably not sufficient to describe the crystallization kinetics during flow. If shear flow is applied at a sufficiently high temperature, dependent on material and applied shear rate, remelting of flow-induced crystalline structures and relaxation of oriented chains is able to (partially) erase the effect of flow. With increasing $\bar{M}_w$, the effect of flow is prevailed longer. Although not investigated in this study, we think that an increased cooling rate (i.e., less time to remelt flow induced structures) will also enlarge the resulting effect of flow.

## References and Notes


(1) Lee, O.; Kamal, M. R. *Polym. Eng. Sci.* **1999**, *39*, 236−248.
(2) Jerschow, P.; Janeschitz-Kriegl, H. *Rheol. Acta* **1996**, *35*, 127−133.
(3) Tribout, C.; Monasse, B.; Haudin, J. M. *Colloid Polym. Sci.* **1996**, *274*, 197−208.
(4) Vleeshouwers, S.; Meijer, H. E. H. *Rheol. Acta* **1996**, *35*, 391−399.
(5) Keller, A.; Kolnaar, J. W. H. In *Processing of Polymers*; Meijer, H. E. H., Ed.; VCH: New York, 1997; Vol. 18, pp 189−268.
(6) Eder, G.; Janeschitz-Kriegl, H. In *Processing of Polymers*; Meijer, H. E. H., Ed.; VCH: New York, 1997; Vol. 18, pp 269−342.
(7) Jay, F.; Haudin, J. M.; Monasse, B. *J. Mater. Sci.* **1999**, *34*, 2089−2102.
(8) Somani, R. H.; Hsiao, B. S.; Nogales, A. *Macromolecules* **2000**, *33*, 9385−9394.
(9) Kumaraswamy, G.; Kornfield, J. A.; Yeh, F.; Hsiao, B. S. *Macromolecules* **2002**, *35*, 1762−1769.
(10) Seki, M.; Thurman, D. W.; Oberhauser, J. P.; Kornfield, J. A. *Macromolecules* **2002**, *35*, 2583−2594.
(11) Koscher, E.; Fulchiron, R. *Polymer* **2002**, *43*, 6931−6942.
(12) Elmoumni, A.; Winter, H. H.; Waddon, A. J. *Macromolecules* **2003**, *36*, 6453−6461.
(13) Janeschitz-Kriegl, H.; Ratajski, E.; Stadlbauer, M. *Rheol. Acta* **2003**, *42*, 355−364.
(14) Swartjes, F. H. M.; Peters, G. W. M.; Rastogi, S.; Meijer, H. E. H. *Int. Polym. Proc.* **2003**, *18*, 53−66.
(15) Fritzsche, A. K.; Price, F. P. *Polym. Eng. Sci.* **1974**, *14*, 401−412.
(16) Fleischmann, E.; Koppelmann, J. *J. Appl. Polym. Sci.* **1990**, *41*, 1115−1121.
(17) Watanabe, K.; Suzuki, T.; Masubuchi, Y.; Taniguchi, T.; Takimoto, J.; Koyama, K. *Polymer* **2003**, *44*, 5843−5849.
(18) Van der Beek, M. H. E.; Peters, G. W. M.; Meijer, H. E. H. *Int. Polym. Proc.* **2005**, *20*, 111−120.
(19) Mezghani, K.; Phillips, P. *Polymer* **1998**, *39*, 3735−3744.
(20) Flory, P. J. *J. Chem. Phys.* **1947**, *15*, 397−408.
(21) Pogodina, N. V.; Lavrenko, V. P.; Srinivas, S.; Winter, H. H. *Polymer* **2001**, *42*, 9031−9043.
(22) Eder, G.; Janeschitz-Kriegl, H.; Liedauer, S. *Prog. Polym. Sci.* **1990**, *15*, 629−714.
(23) Zuidema, H.; Peters, G. W. M.; Meijer, H. E. H. *J. Appl. Polym. Sci.* **2001**, *82*, 1170−1186.
(24) La Carrubba, V.; Brucato, V.; Piccarolo, S. *J. Polym. Sci., Part B: Polym. Phys.* **2002**, *40*, 153−175.
(25) Van der Beek, M. H. E.; Peters, G. W. M.; Meijer, H. E. H. *Macromol. Mater. Eng.* **2005**, *290*, 443−455.
(26) Jerschow, P.; Janeschitz-Kriegl, H. *Int. Polym. Proc.* **1997**, *12*, 72−77.
(27) Janeschitz-Kriegl, H.; Ratasjski, E.; Wippel, H. *Colloid Polym. Sci.* **1999**, *277*, 217−226.
(28) Wilchinsky, Z. W. *J. Appl. Phys.* **1960**, *31*, 1969−1972.
(29) Fujiyama, M.; Wakino, T. *J. Appl. Polym. Sci.* **1988**, *35*, 29−49.
(30) Fujiyama, M.; Wakino, T. J. *J. Appl. Polym. Sci.* **1991**, *43*, 57−81.
(31) Somani, R. H.; Hsiao, B. S.; Nogales, A.; Fruitwala, H.; Srinivas, S.; Tsou, A. H. *Macromolecules* **2001**, *34*, 5902−5909.
(32) Van der Burgt, F. P. T. J.; Rastogi, S.; Chadwick, J. C.; Rieger, B. J. *J. Macromol. Sci., Part B: Phys.* **2002**, *B41*, 1091−1104.
(33) Lovinger, A. J.; Chua, J. O.; Gryte, C. C. *J. Polym. Sci., Polym. Phys.* **1977**, *15*, 641.
(34) Lovinger, A. J. *J. Polym. Sci., Polym. Phys.* **1983**, *21*, 97−110.
(35) Varga, J.; Karger-Kocsis, J. *Polymer* **1995**, *36*, 4877−4881.
(36) Varga, J.; Karger-Kocsis, J. *J. Polym. Sci., Polym. Phys.* **1996**, *34*, 657−670.


MA051914E